Chemical Imaging of Cathode–Electrolyte Interphase in Sulfide Solid-State Batteries

Lihong Zhao[†], Qiuyi Yuan[†], Chaoshan Wu, Takanori Itoh, Suusaku Ogiu, Takashi Sanada, Shohei Yamashita, Daisuke Shibata, Yan Yao[*]*

[a] Lihong Zhao, Chaoshan Wu, Yan Yao

Department of Electrical and Computer Engineering, and Texas Center for Superconductivity at the University of Houston, University of Houston, Texas 77204, USA.

[b] Yan Yao

Energy Storage Research Alliance, Argonne National Laboratory, 9700 South Cass Avenue, Lemont, IL 60439, USA

[c] Qiuyi Yuan, Takanori Itoh, Suusaku Ogiu, Takashi Sanada

Nissan ARC LTD., 1 Natsushima-cho, Yokosuka, Kanagawa, 2370061, Japan.

[d] Shohei Yamashita

IMSS, KEK, 1-1 Oho, Tsukuba, Ibaraki, 3050801, Japan

[e] Daisuke Shibata

SR center, Research Organization of Science and Technology, Ritsumeikan University, 1-1-1 Noji-Higashi, Kusatsu City, Shiga, 5258577, Japan

† L.Z. and Q.Y contributed equally.

Corresponding Author

*Qiuyi Yuan, Email: q-yuan@nissan-arc.co.jp

*Yan Yao, Email: yyao4@uh.edu

ABSTRACT

The cathode–electrolyte interphase critically impacts the performance of solid-state batteries, yet its chemical evolution remains poorly understood, especially in sulfide systems. Here, we employ scanning transmission X-ray microscopy (STXM) to directly map the NMC–argyrodite interphase. We show that sulfide oxidation primarily occurs at the electrolyte surrounding NMC particles, while the bulk electrolyte remains electrochemically stable. This interfacial oxidation, accompanied by Ni reduction, leads to the formation of S^0 and SO_x^{2-} species that drive high-impedance interphase growth. Our results provide direct evidence of cathode–electrolyte interactions and a clear visualization of interfacial degradation.

Keywords: scanning transmission X-ray microscopy; chemical mapping; solid-state battery; composite cathode; interphase

All-solid-state batteries (ASSBs) offer enhanced safety and the potential for higher energy density.[1–3] A composite cathode, typically comprised of active material, solid electrolyte, and conductive carbon, plays a pivotal role in determining cell energy density and rate capability.[4–7] To achieve optimal performance, the solid electrolyte within the cathode should exhibit high ionic conductivity to compensate for its tortuous structure, low mass density to reduce the weight fraction of inactive components, and good contact with the cathode to minimize interfacial resistance.[1,8] Sulfide electrolytes stand out as promising candidates for ASSBs due to their high Li-ion conductivity, moderate mass density, and excellent processability, which facilitate good interfacial contact.[9,10] However, sulfides are often plagued by interfacial side reactions, especially at high electrochemical potentials.[11] Understanding these reactions and the distribution of reaction products is critical to improve overall battery performance.

Extensive studies have characterized interfacial side reactions between sulfide electrolyte and oxide cathodes. It is well established that sulfide (S^{2-}) undergoes oxidation to elemental sulfur (S^0) at high potentials.[11–13] Sulfur can then further oxidize into sulfites and sulfates in the presence of oxide cathodes during charging.[14] The resulting cathode–electrolyte interphase (CEI) hinders ion transport between the active material and the electrolyte, leading to increased impedance and overpotential during cycling.

Despite the critical role of the CEI in composite cathodes, little progress has been made in clarifying its origin—specifically, whether it arises solely from high electrochemical potential or from coupled chemical and electrochemical reactions. A major challenge lies in accurately probing redox species at the interface and in the adjacent electrolyte and layered oxide cathodes. Conventional techniques such as X-ray photoelectron spectroscopy (XPS) offer only limited insights, since they average oxidation states over relatively large beam spots. Furthermore, layered

oxide particles show inter-particle and intra-particle heterogeneity in state-of-charge (SoC),[15,16,17] making bulk chemical measurements better suited to capturing overall reaction trends than to pinpointing the precise chemical processes at the interphase.

Other high-resolution methods also face limitations. Electron beam-based techniques such as scanning electron microscopy (SEM) and transmission electron microscopy (TEM) provide elemental information but lack sensitivity to chemical valence states.[18] Although electron energy-loss spectroscopy provides information on chemical states, sulfide electrolytes are highly susceptible to beam damage in TEM, restricting most observations to residual electrolyte near active materials, even with lamella samples.[19] Optical spectroscopy methods generally lack the spatial resolution required to probe nanoscale interfacial features.[20] Time-of-flight secondary ion mass spectrometry (ToF-SIMS) can detect fragments of interfacial side products and visualize CEI around active material particles,[21,22] but it cannot definitively resolve their chemical states.

Scanning X-ray imaging has emerged as a promising technique for mapping the evolution of chemical states in battery systems with high spatial resolution.[23–25] It has been used to track lithiation states in individual cathode particles[16,17,26,27] and to probe degradation at cathode–electrolyte interfaces in semi-solid [28,29] and solid polymer batteries.[30] However, due to challenges in sample preparation and the limited availability of soft X-ray sources, scanning transmission X-ray microscopy (STXM) has not yet been widely applied to sulfide-based solid electrolytes.

In this work, we employ STXM to visualize chemical state evolution in composite cathodes of sulfide-based ASSBs. We provide direct evidence of sulfide oxidation and nickel reduction at the cathode–electrolyte interphase, validating mechanisms previously inferred from indirect characterization. By mapping the oxidation state of sulfur within the composite cathode, we reveal

that high electrochemical potential alone is insufficient to degrade sulfide electrolytes; instead, degradation is strongly facilitated by the presence of cathode active materials.

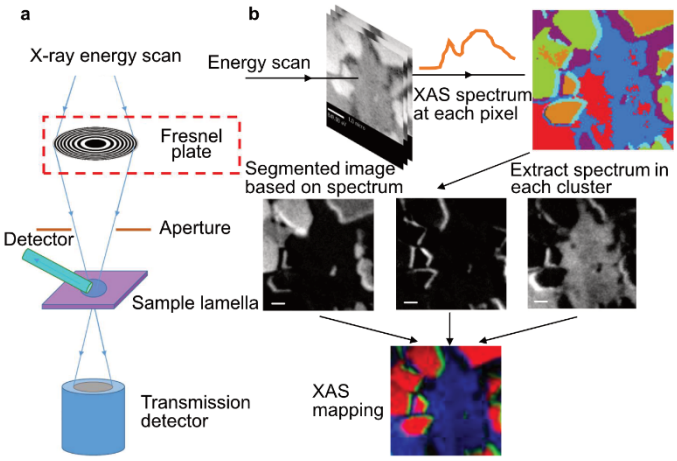

Figure 1. Chemical mapping of composite cathodes. (a) Schematic illustration of the STXM measurement; (b) Flowchart of the characterization procedure. The composite cathode was prepared into a lamella using FIB-SEM, followed by XAS spectrum acquisition at each pixel. The resulting images were segmented based on spectral features using SVD to generate the XAS map.

NMC-argyrodite degradation at high cutoff voltage

STXM was used to directly visualize the chemical states of both cathode and electrolyte components at the nanoscale. **Figure 1** schematically illustrates the imaging procedure and data collection process. The composite cathode was thinned into a ~100 nm lamella and transferred to the STXM chamber under Ar protection. At each scan step, X-ray transmission was acquired, and singular value decomposition (SVD) was applied to segment images based on spectral variations, enabling chemical mapping of the imaged region. We used NMC83 ($LiNi_{0.83}Mn_{0.06}Co_{0.11}O_2$) and argyrodite ($Li_6PS_5Cl$) as a model system to study cathode – electrolyte interphase formation.

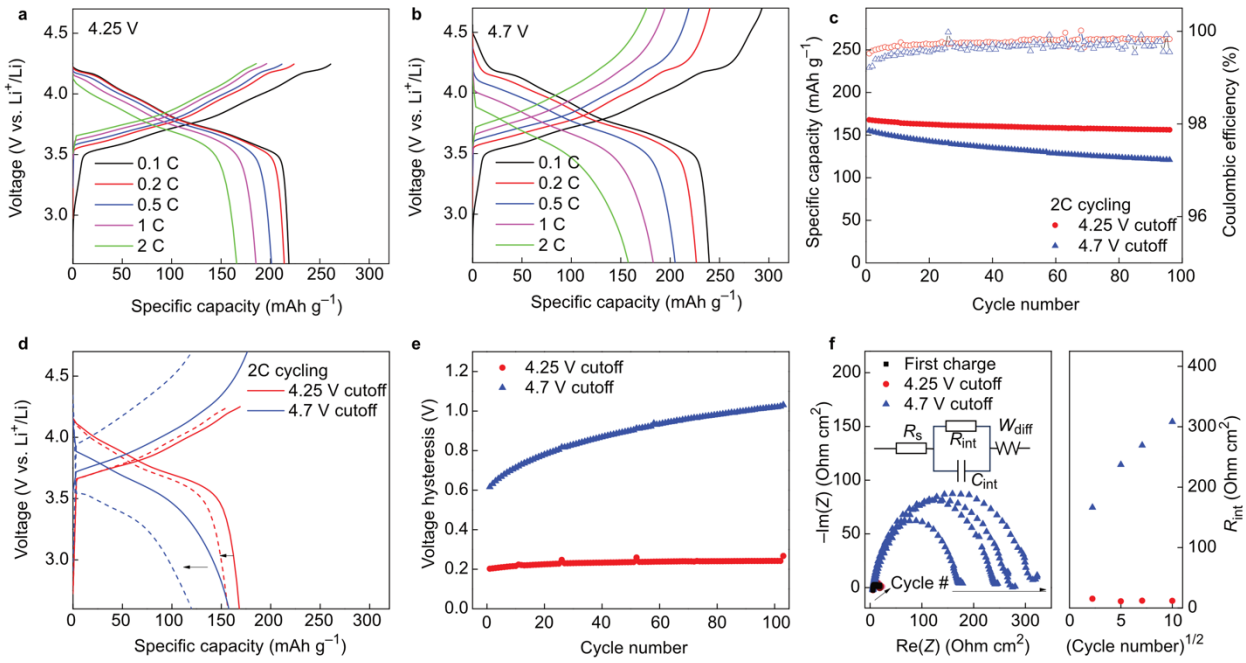

Figure 2. Electrochemical performance of the NMC-argyrodite cathode at different cutoff voltages. (a) Voltage profile at 4.25 V cutoff; (b) voltage profile at 4.7 V cutoff; (c) capacity retention over 100 cycles at 2C; (d) capacity and voltage decay from the 1st to 100th cycle at 2C; (e) voltage hysteresis over 100 cycles at 2C; (f) electrochemical impedance at 5th, 25th, 50th, and 100th cycles, measured at fully charged state. The inset shows the equivalent circuit model. The charge-transfer resistance increases linearly with the square root of the cycle number.

To study cathode–electrolyte interphase (CEI) formation, the composite cathode was intentionally subjected to harsh cycling. As a baseline, cells were cycled between 2.6–4.25 V vs. Li^+/Li. Voltage profiles (**Figure 2a**) and capacity retention curves (**Figure 2c**) showed reasonable performance: a reversible capacity at 218 mAh/g at 0.1 C, initial Coulombic efficiency (ICE) of 84%, and 93% capacity retention after 100 cycles at 2C.

Increasing the cutoff to 4.7 V vs. Li^+/Li (**Figure 2b**) boosted the first-cycle discharge capacity to 239 mAh/g with ICE of 81%, but capacity faded rapidly, retaining only 77% after 100

cycles (**Figure 2d**). Cycling at 4.7 V also induced stronger voltage hysteresis (**Figure 2e**). At 4.25 V cutoff, the average discharge potential was 0.2 V lower than the average charge potential; at 4.7 V, this difference expanded from 0.6 to 1.0 V over 100 cycles, indicating progressive interfacial impedance. Cross-section imaging after cycling (**Figure S1**) revealed minor cracks within NMC and partial loss of contact at the NMC–SE interface, while the overall composite structure remained intact.

Electrochemical impedance spectra collected at 4.25 V vs. Li^+/Li after the 5^{th}, 25^{th}, 50^{th}, and 100^{th} cycle (**Figure 2f**) reinforced these findings. The impedance of cells cycled to 4.25 V cutoff remained nearly unchanged, whereas those cycled to 4.7 V exhibited rapid growth. Interfacial resistance (R_{int}) increased linearly with the square root of cycle number, consistent with the classical solid–electrolyte interphase (SEI) growth model, which suggests the evolution of an electronically insulating but ionically conductive interphase.[31,32]

Shift in Ni and S oxidation state at the interface

The chemical state evolution of NMC and argyrodite was investigated using X-ray absorption spectroscopy (XAS) in different detection modes (**Figure 3a**). Total electron yield (TEY) probes the surface (~10 nm), partial fluorescence yield (PFY) and inverse partial fluorescence yield (IPFY) capture subsurface signals (~hundreds of nm), while STXM detects bulk

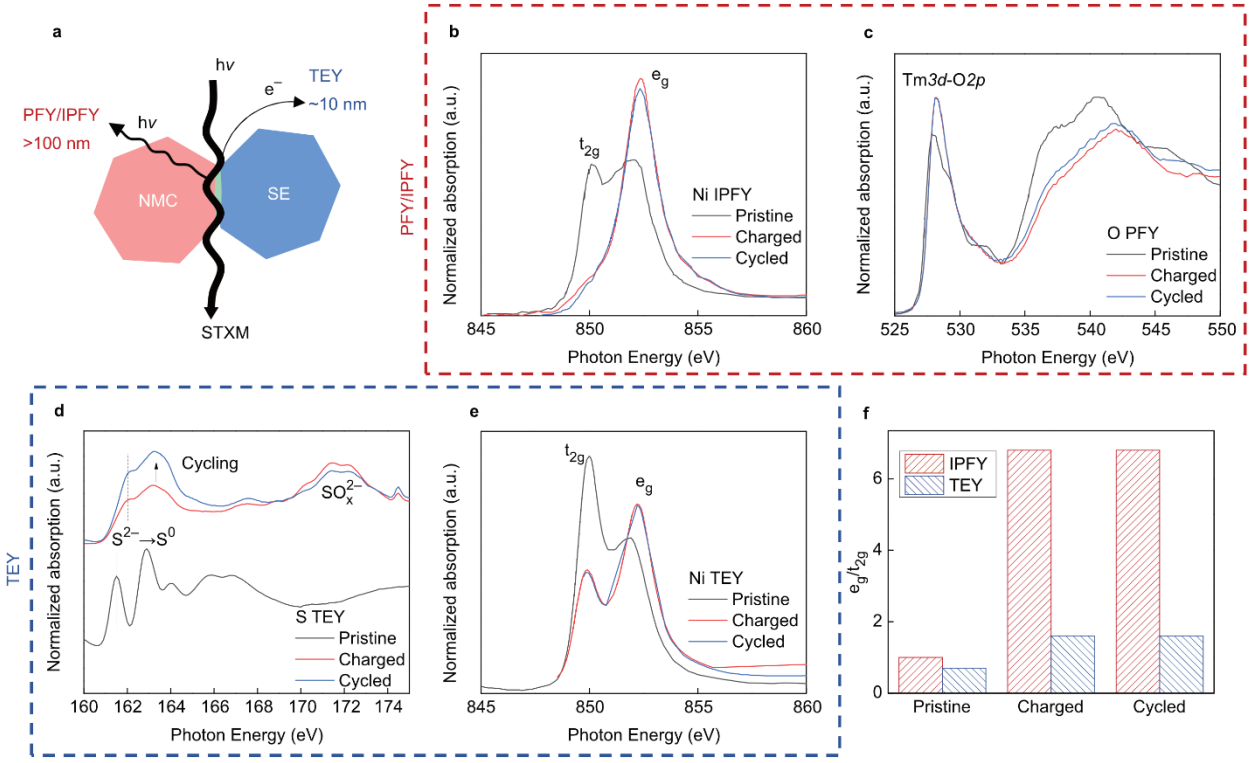

Figure 3. X-ray absorption spectra of composite cathodes. (a) Schematic illustration of the probing depth of PFY/IPFY, TEY, and STXM measurements; (b) Ni IPFY spectra; (c) O PFY spectra; (d) S TEY spectra; (e) Ni TEY spectra; (f) e_g/t_{2g} ratio of Ni. The pristine sample (black) corresponds to the NMC-argyrodite composite cathode at 2.6 V vs. Li^+/Li. The charged sample (red) represents the cathode charged to 4.25 V vs. Li^+/Li during the first charge. The cycled sample (blue) represents the cathode after 100 cycles between 2.6–4.25 V vs. Li^+/Li, followed by a final charge to 4.25 V vs. Li^+/Li.

transmission.[16] Here, we employed Ni-L edge IPFY to eliminate the self-absorption effect inherent to PFY owing to its high concentration.[33]

XAS spectra were compared for three conditions: the pristine sample (2.6 V vs. Li^+/Li), the charged sample (first charged to 4.25 V vs. Li^+/Li), and the cycled sample (100 cycles at 4.25 V, followed by charging to 4.25 V vs. Li^+/Li). In Ni IPFY spectra (**Figure 3b**), two peaks at 850

eV and 852 eV correspond to t_{2g} and e_g states, respectively. A higher e_g/t_{2g} ratio indicates a higher oxidation state.[34] For the charged samples, the e_g/t_{2g} ratio was ~6.8, significantly higher than the value of ~1.0 in the pristine state (**Figure 3f**). A similar trend appeared in Ni TEY spectra (**Figure 3e**), though with lower ratios of 1.6 (charged) and 0.7 (pristine), suggesting that the NMC surface is more reduced than the bulk, likely due to interactions with the sulfide electrolyte.

O K-edge PFY spectra (**Figure 3c)** exhibited a pre-edge feature at 528 eV, corresponding to hybridization between transition metal 3d and oxygen 2p orbitals, along with main-edge features above 535 eV.[35] A minor peak at 532.5 eV is attributed to surface Li_2CO_3.[36] A larger pre-edge peak area correlated with higher transition metal oxidation states, consistent with the Ni-L edge results showing Ni oxidation upon charging.

In S L-edge TEY spectra, both charge state and cycling history significantly influence spectral features. In the pristine state, two peaks at 161.5 and 162.8 eV are consistent with S^{2-}. Upon charging, regardless of cycling history, these peaks shifted to 162.0 and 163.3 eV, reflecting decreased electron density around sulfur and indicating oxidation of S^{2-} to S^0.[37] Additional peaks at ~172 eV correspond to SO_x^{2-} species.[38]

Together, these spectroscopy measurements establish a baseline for STXM analysis. Bulk spectroscopy reveals that surface sulfur oxidizes to S^0 and SO_x^{2-} upon charging, with little dependence on cycling. On the cathode side, Ni shows a lower oxidation state at the surface (~10 nm) compared to the subsurface (~ hundreds of nm), likely due to interfacial side reactions between NMC with the sulfide electrolyte.

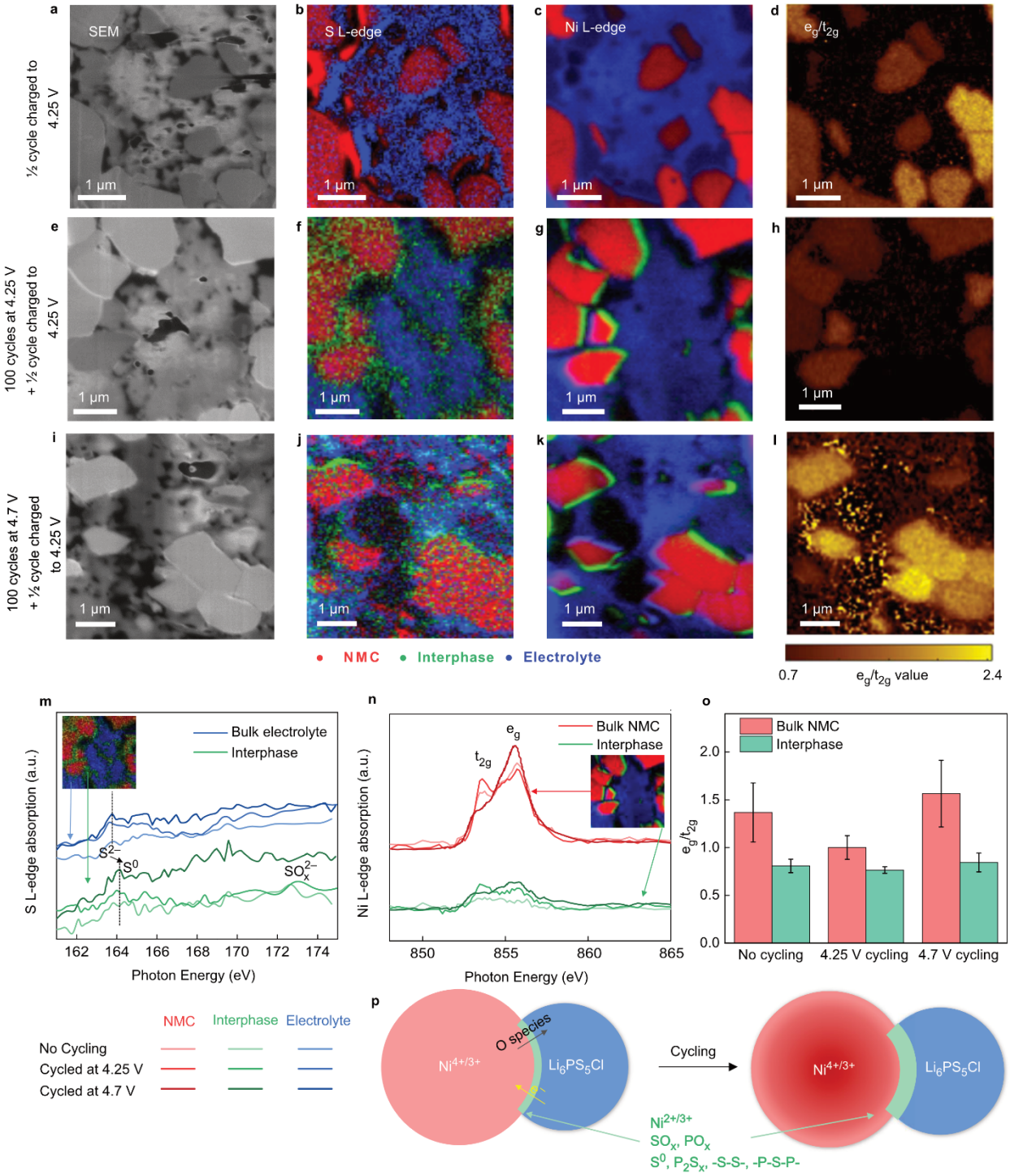

Figure 4. XAS mapping of the NMC–argyrodite interface. (a-d) SEM, S L-edge, Ni L-edge, and Ni e_g/t_{2g} mapping of an NMC-Li_6PS_5Cl laminate charged to 4.25 V vs. Li^+/Li without cycling; (e-h) corresponding maps of a laminate charged to 4.25 V after 100 cycles at 4.25 V; (i-l) corresponding maps of a laminate at charged state 4.25 V after 100 cycles at 4.7 V. Red, green, and blue regions correspond to NMC, the interphase, and the electrolyte, respectively. (m) S L-edge and (n) Ni L-edge spectra collected from bulk NMC (red), interphase (green), and bulk electrolyte (blue) region; inset indicates the representative sampling locations. Line colors with varying lightness correspond to different samples, as shown at the bottom right of the panel. (o) Ni e_g/t_{2g} ratio extracted from bulk NMC (red) and interphase (green) regions; error bars represent standard deviation across particles. (p) Schematic illustration of the interfacial reaction between NMC and argyrodite.

Chemical imaging of cathode–electrolyte interphase

To simultaneously observe the solid electrolyte and active material, S- and Ni-L edges were selected for STXM characterization. **Figure 4** maps the evolution of the chemical state at the electrode level. Three conditions were compared at the charged state (4.25 V vs. Li^+/Li): without prior cycling (**Figure 4a–d**), after 100 cycles at 4.25 V cutoff (**Figure 4e–h**), and after 100 cycles at 4.7 V cutoff (**Figure 4i–l**). In SEM images (**Figure 4a,e,i**), smooth, dense regions correspond to single-crystalline NMC, while porous regions represent the solid electrolyte. Although all three lamellae show similar morphology, the sample cycled to 4.7 V displays large transverse cracks (**Figure S1**), likely caused by the reversible volume change of NMC (~5%) and irreversible electrolyte expansion driven by chemical and electrochemical side reactions.[39,40]

Interfacial reactions are revealed by S L-edge mapping. In the bulk electrolyte (blue), the S L-edge consistently shows a low-energy peak at 161.5 eV across all samples, characteristic of S^{2-} in argyrodite. These spectra closely resemble the TEY spectrum of pristine electrolyte, indicating minimal side reactions within bulk electrolyte particles. At the interphase (green) between NMC and electrolyte, however, the S L-edge shifts to higher energy (162.8 eV), consistent with the formation of S^0. Higher-valence sulfur species (SO_x^{2-}) are also detected. Despite the presence of conductive carbon in the composite cathode, no electrolyte oxidation was observed in the bulk, suggesting that sulfide degradation is unlikely to occur solely due to high potential. Instead, active materials such as NMC are required to drive interfacial sulfide oxidation. While oxygen release from oxide cathodes at high voltage has been widely reported, no shift in the O K-edge was detected in either bulk spectra (**Figure 3c, f**) or STXM measurements (**Figure S2**). This suggests that released oxygen reacts immediately with the sulfide electrolyte, forming an interphase and suppressing detectable oxygen signals.

The interphase thickness evolves with cycling. After a single charge to 4.25 V, only a negligible interphase was detected, thinner than the STXM spatial resolution (50 nm), as no distinct region emerged in SVD fitting. After 100 cycles, however, the interfacial region expanded significantly **(Figure 4f, j**), contributing to voltage hysteresis and increased impedance.

Alongside sulfur oxidation, Ni reduction at the interphase is evident. The e_g/t_{2g} ratio is consistently lower at the interphase (green) than in bulk NMC (red) (**Figure 4n, o)**. After one charge to 4.25 V, no interfacial Ni reduction was observed (**Figure 4c**). After 100 cycles, however, the interphase thickened to 100–200 nm for both cutoff voltages (**Figure 4g, k**), with clear decreases in Ni valence localized at the NMC-argyrodite boundary. Notably, Ni valence at internal NMC grain boundaries remained unchanged, as indicated by the uniform red contrast in **Figure**

4k. Mapping by the Ni e_g/t_{2g} ratio (**Figure 4d, h**, **l)** highlights a darker contrast at NMC surfaces adjacent to the electrolyte, reflecting localized reduction.

Interestingly, individual NMC particles show different states of charge, reflecting particle-level heterogeneity in the composite cathode. Such heterogeneity arises from uneven access to ionic and electronic transport pathways due to the complex cathode microstructure.

Overall, chemical mapping directly supports the proposed cathode degradation mechanism (**Figure 4p**). Repeated cycling, especially at high cutoff voltages, leads to sulfide oxidation at the NMC surface, while the bulk electrolyte remains stable despite conductive carbon and high potential. Oxygen released from NMC likely accelerates electrolyte oxidization near active particles.[41] Concurrently, interfacial Ni reduction occurs, producing an increasingly thick interphase. Over time, this process raises impedance and voltage hysteresis, ultimately limiting electrochemical performance.

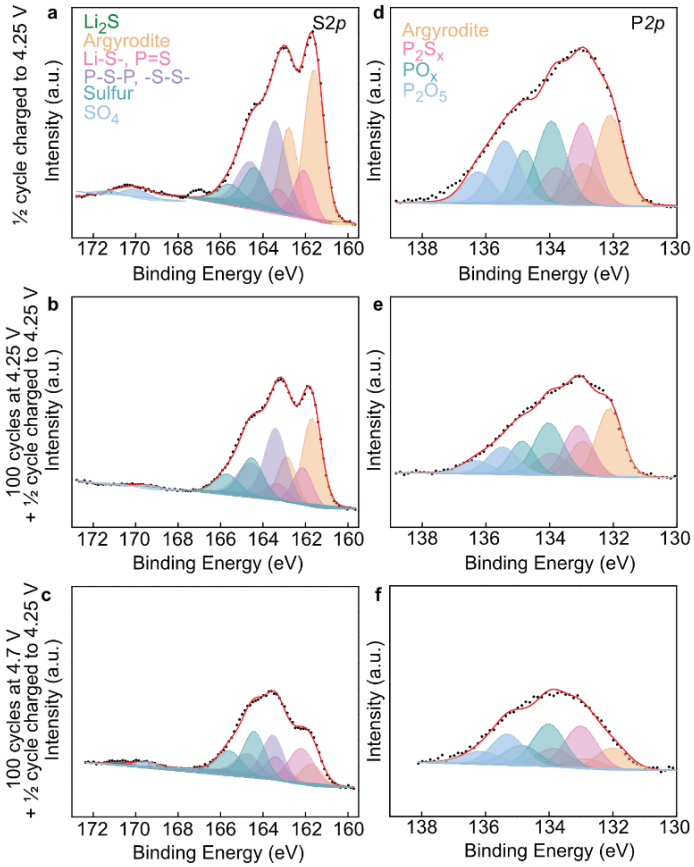

Figure 5. XPS spectra of NMC–argyrodite interphase. (a–c) phosphorous spectra at charged state (4.25 V vs. Li^+/Li) with no extra cycling (a), 100 cycles at 4.25 V (b), and 100 cycles at 4.7 V (c), respectively; (d–f) Sulfur spectra at charged state (4.25 V vs. Li^+/Li) with no extra cycling (d), 100 cycles at 4.25 V (e), and 100 cycles at 4.7 V (f), respectively.

Interfacial chemical reactions were further confirmed by XPS of composite cathodes at the charged state. After 100 cycles at 4.25 V and 4.7 V, the S 2p peak for argyrodite (161.7 eV) reduced from 42% to 33% and 13%, respectively, while the S^0 content (164.4 eV) increased from 12% to 17% and 28% (**Figure 5a–c, Table S1**). The contribution of SO_4^{2-} (169.2 eV) remained consistently low (2–3%). These results align with XAS and STXM (Figures 3 and 4), confirming S^0 as the primary side product. A similar trend appeared in P 2p spectra: argyrodite (132.0 eV)

decreased from 33% to 16%, while P_2S_x (133.0 eV) and PO_x (134.0 eV) slightly increased after cycling (**Figure 5d–f**, **Table S2**).

In summary, we directly visualized interfacial degradation in NMC-argyrodite composite cathodes for solid-state batteries using STXM chemical mapping. High-voltage cycling accelerates sulfide oxidation at the NMC interface, forming S^0 and SO_x^{2-} while the bulk electrolyte remains stable. Concurrently, interfacial Ni reduction occurs. Progressive interphase growth raises impedance, leading to capacity fade and voltage hysteresis. This work provides clear evidence of cathode–electrolyte reactions and a straightforward visualization of interfacial degradation.

Experimental Methods

Materials and electrode fabrication. Single-crystal $LiNi_{0.83}Mn_{0.06}Co_{0.11}O_2$ (NMC, MSE Supplies) was used as the cathode active material, Li_6PS_5Cl (LPSCl, MSE Supplies) was used in the solid electrolyte and in the composite cathode, vapor grown carbon fibers (VGCF) (PR-19-XT-HHT, Applied Sciences) was used as a conductive additive, and PTFE (Sigma) was used as binder for composite cathode fabrication. PTFE binder is mandatory to maintain mechanical integrity of FIB-cut cathode lamella. Li-Mg foil (90 µm, MSE Supplies) was used as the anode, with nearly identical electrode potential compared to Li (1 mV vs. Li^+/Li) while providing better stability at high current densities. NMC, LPSCl, VGCF, and PTFE were mixed in mass ratio of 70:27:3:0.5 in a hot mortar and pestle to fibrilize the binder. The mixture was further rolled with a metal rod on a hot plate to achieve desired thickness and finally tailored to an 11.1 mm free-standing disk.

Electrochemical characterization of full cells. Electrochemical tests were carried out in polyether-ether-ketone (PEEK) die cells with a diameter of 12.7 mm. Typically, 130 mg solid electrolyte powder was compressed in the die under 150 MPa to form a pellet. Composite cathode disk (8.89 mg active material, 1.4 mAh cm^{-2}) was placed on one side of the solid electrolyte and further densified at 375 MPa. After densification, a piece of ~90 μm Li-Mg foil was added to the counter side and further pressed at 50 MPa for 1 minute to improve interfacial contact. The cell is subject to a stack pressure of 14 MPa. All evaluations were done at a temperature of 60 °C within a climate-controlled oven using VMP-3 potentiostat. Electrochemical impedance spectrum was collected from 1 MHz to 100 mHz at 7 mV amplitude. For samples at charged state, the cell was charged to 4.25 V vs. Li^+/Li at 0.1 C. For cycled cathode, the cell was cycled at 2 C rate with 4.25 V and 4.7 V cutoff voltages for 100 cycles, then charged to 4.25 V at 0.1 C to maintain consistency in sample state-of-charge. Pellet cells were removed from PEEK die and cut into 3 pieces using ceramic cutter for STXM, XAS and XPS characterizations.

STXM characterization. To allow the X-ray being able to transmit at S-L and Ni-L edge, the pellet cells were cut into 100 nm-thick lamella with the area of 7×7 μm using cryogenic plasma-FIB (Helios G4 PFIB Cxe, Thermo Scientific) using the acceleration voltage of 30 KeV. The STXM experiment was conducted at BL-19A, Photon Factory, KEK (**Figure S3**). Incident X-ray was focused through Fresnel zone plate. aXis2000 was used for STXM data processing and SVD analysis.[42] All transfer and characterization including PFIB were carried out under Ar protection.

XAS characterization. S-L and Ni-L edge PFY/IPFY and TEY spectra were collected from the top surface of composite cathode at BL-11, SR center, Ritsumeikan University with grating as monochromator. A transfer vessel was used to protect the samples from air during transportation. All spectra were processed using Athena for background removal and normalization.[43]

XPS characterization. All samples were transferred to XPS (VersaProbeIII, ULVAC-PHI) using a transfer vessel to protect the sample from air. XPS was measured using monochromized Al-K α source (1486.6 eV), with the beam size of Φ200 μm. Spectra scans were taken under the condition of 50 W power, 45° take-off angle and pass energy of 69 eV. Peak fitting was carried out using MultiPak using Shirley for background removal.

Supporting Information

Supporting information contains detailed XPS analysis, postmortem SEM of composite cathode, O K-edge XAS and experimental setup.

AUTHOR INFORMATION

Correspondence and requests for materials should be addressed to Qiuyi Yuan (q-yuan@nissan-arc.co.jp) or Yan Yao (yyao4@uh.edu).

NOTES

Y.Y. has equity interest in LiBeyond, LLC and Solid Design Instruments, LLC. The University of Houston reviewed and approved his relationship in compliance with its conflict-of-interest policy. The remaining authors declare no competing interests.

ACKNOWLEDGEMENTS

This work is funded by the Energy Storage Research Alliance "ESRA" (DE-AC02-06CH11357), an Energy Innovation Hub funded by the U.S. Department of Energy, Office of Science, Basic Energy Sciences. STXM experiment was carried out under the approval of PAC No. 2021G592 and XAS was under Proposal No. S22011 of Ritsumeikan SR center.

REFERENCES

(1) Janek, J.; Zeier, W. G. Challenges in Speeding up Solid-State Battery Development. *Nat. Energy* **2023**, *8* (3), 230–240. https://doi.org/10.1038/s41560-023-01208-9.

(2) Zhao, L.; Lakraychi, A. E.; Chen, Z.; Liang, Y.; Yao, Y. Roadmap of Solid-State Lithium-Organic Batteries toward 500 Wh Kg^{-1}. *ACS Energy Lett* **2021**, *6* (9), 3287–3306. https://doi.org/10.1021/acsenergylett.1c01368.

(3) Guo, L.; Zheng, J.; Zhao, L.; Yao, Y. Interfacial Instabilities in Halide-Based Solid-State Batteries. *MRS Bull.* **2023**, *48* (12), 1247–1256. https://doi.org/10.1557/s43577-023-00607-3.

(4) Zhang, J.; Chen, Z.; Ai, Q.; Terlier, T.; Hao, F.; Liang, Y.; Guo, H.; Lou, J.; Yao, Y. Microstructure Engineering of Solid-State Composite Cathode via Solvent-Assisted Processing. *Joule* **2021**, *5* (7), 1845-1859. https://doi.org/10.1016/j.joule.2021.05.017

(5) Le, M.; Yao, A.; Zhang, A.; Le, H.; Chen, Z.; Wu, X.; Zhao, L.; Chen, J.; Zhao, L. Expediting Ionic Conductivity Prediction of Solid-State Battery Electrodes Using Machine Learning. *IEEE J. Multiscale Multiphysics Comput. Tech.* **2024**, *9*, 375–382. https://doi.org/10.1109/jmmct.2024.3475988.

(6) Hao, F.; Liang, Y.; Zhang, Y.; Chen, Z.; Zhang, J.; Ai, Q.; Guo, H.; Fan, Z.; Lou, J.; Yao, Y. High-Energy All-Solid-State Organic–Lithium Batteries Based on Ceramic Electrolytes. *ACS Energy Lett.* **2020**, *6* (1), 201–207. https://doi.org/10.1021/acsenergylett.0c02227.

(7) Hao, F.; Chi, X.; Liang, Y.; Zhang, Y.; Xu, R.; Guo, H.; Terlier, T.; Dong, H.; Zhao, K.; Lou, J.; Yao, Y. Taming Active Material-Solid Electrolyte Interfaces with Organic Cathode for All-Solid-State Batteries. *Joule* **2019**, *3* (5), 1349–1359. https://doi.org/10.1016/j.joule.2019.03.017.

(8) Shi, T.; Tu, Q.; Tian, Y.; Xiao, Y.; Miara, L. J.; Kononova, O.; Ceder, G. High Active Material Loading in All-Solid-State Battery Electrode via Particle Size Optimization. *Adv. Energy Mater.* **2020**, *10* (1), 1902881. https://doi.org/10.1002/aenm.201902881.

(9) Wu, C.; Lou, J.; Zhang, J.; Chen, Z.; Kakar, A.; Emley, B.; Ai, Q.; Guo, H.; Liang, Y.; Lou, J.; Yao, Y.; Fan, Z. Current Status and Future Directions of All-Solid-State Batteries with Lithium Metal Anodes, Sulfide Electrolytes, and Layered Ternary Oxide Cathodes. *Nano Energy* **2021**, *87*, 106081. https://doi.org/10.1016/j.nanoen.2021.106081.

(10) Tan, D. H. S.; Meng, Y. S.; Jang, J. Scaling up High-Energy-Density Sulfidic Solid-State Batteries: A Lab-to-Pilot Perspective. *Joule* **2022**, *6* (8), 1755–1769. https://doi.org/10.1016/j.joule.2022.07.002.

(11) Schwietert, T. K.; Arszelewska, V. A.; Wang, C.; Yu, C.; Vasileiadis, A.; Klerk, N. J. J. de; Hageman, J.; Hupfer, T.; Kerkamm, I.; Xu, Y.; Maas, E. van der; Kelder, E. M.; Ganapathy, S.; Wagemaker, M. Clarifying the Relationship between Redox Activity and Electrochemical Stability in Solid Electrolytes. *Nat. Mater.* **2020**, *19* (4), 428–435. https://doi.org/10.1038/s41563-019-0576-0.

(12) Minnmann, P.; Quillman, L.; Burkhardt, S.; Richter, F. H.; Janek, J. Editors' Choice—Quantifying the Impact of Charge Transport Bottlenecks in Composite Cathodes of All-Solid-State Batteries. *J. Electrochem. Soc.* **2021**, *168* (4), 040537. https://doi.org/10.1149/1945-7111/abf8d7.

(13) Jung, S.-K.; Gwon, H.; Lee, S.-S.; Kim, H.; Lee, J. C.; Chung, J. G.; Park, S. Y.; Aihara, Y.; Im, D. Understanding the Effects of Chemical Reactions at the Cathode–Electrolyte Interface in Sulfide Based All-Solid-State Batteries. *J. Mater. Chem. A* **2019**, *7* (40), 22967–22976. https://doi.org/10.1039/c9ta08517c.

(14) Walther, F.; Koerver, R.; Fuchs, T.; Ohno, S.; Sann, J.; Rohnke, M.; Zeier, W. G.; Janek, J. Visualization of the Interfacial Decomposition of Composite Cathodes in Argyrodite-Based All-Solid-State Batteries Using Time-of-Flight Secondary-Ion Mass Spectrometry. *Chem. Mater.* **2019**, *31* (10), 3745–3755. https://doi.org/10.1021/acs.chemmater.9b00770.

(15) Yang, Z.; Lin, F. Heterogeneous, Defect-Rich Battery Particles and Electrodes: Why Do They Matter, and How Can One Leverage Them? *J. Phys. Chem. C* **2021**, *125* (18), 9618–9629. https://doi.org/10.1021/acs.jpcc.1c01703.

(16) Gent, W. E.; Lim, K.; Liang, Y.; Li, Q.; Barnes, T.; Ahn, S.-J.; Stone, K. H.; McIntire, M.; Hong, J.; Song, J. H.; Li, Y.; Mehta, A.; Ermon, S.; Tyliszczak, T.; Kilcoyne, D.; Vine, D.; Park, J.-H.; Doo, S.-K.; Toney, M. F.; Yang, W.; Prendergast, D.; Chueh, W. C. Coupling between Oxygen Redox and Cation Migration Explains Unusual Electrochemistry in Lithium-Rich Layered Oxides. *Nat. Commun.* **2017**, *8* (1), 2091. https://doi.org/10.1038/s41467-017-02041-x.

(17) Park, J.; Zhao, H.; Kang, S. D.; Lim, K.; Chen, C.-C.; Yu, Y.-S.; Braatz, R. D.; Shapiro, D. A.; Hong, J.; Toney, M. F.; Bazant, M. Z.; Chueh, W. C. Fictitious Phase Separation in Li Layered Oxides Driven by Electro-Autocatalysis. *Nat. Mater.* **2021**, *20* (7), 991–999. https://doi.org/10.1038/s41563-021-00936-1.

(18) Liu, G.; Lu, Y.; Wan, H.; Weng, W.; Cai, L.; Li, Z.; Que, X.; Liu, H.; Yao, X. Passivation of the Cathode–Electrolyte Interface for 5 V-Class All-Solid-State Batteries. *ACS Appl. Mater. Interfaces* **2020**, *12* (25), 28083–28090. https://doi.org/10.1021/acsami.0c03610.

(19) Zhang, R.; Strauss, F.; Jiang, L.; Casalena, L.; Li, L.; Janek, J.; Kondrakov, A.; Brezesinski, T. Transition-Metal Interdiffusion and Solid Electrolyte Poisoning in All-Solid-State Batteries Revealed by Cryo-TEM. *Chem. Commun.* **2023**, *59* (31), 4600–4603. https://doi.org/10.1039/d3cc00516j.

(20) Lou, S.; Yu, Z.; Liu, Q.; Wang, H.; Chen, M.; Wang, J. Multi-Scale Imaging of Solid-State Battery Interfaces: From Atomic Scale to Macroscopic Scale. *Chem* **2020**, *6* (9), 2199–2218. https://doi.org/10.1016/j.chempr.2020.06.030.

(21) Ai, Q.; Chen, Z.; Zhang, B.; Wang, F.; Zhai, T.; Liu, Y.; Zhu, Y.; Terlier, T.; Fang, Q.; Liang, Y.; Zhao, L.; Wu, C.; Guo, H.; Fan, Z.; Tang, M.; Yao, Y.; Lou, J. High-Spatial-Resolution Quantitative Chemomechanical Mapping of Organic Composite Cathodes for Sulfide-Based Solid-State Batteries. *ACS Energy Lett.* **2023**, *8* (2), 1107–1113. https://doi.org/10.1021/acsenergylett.2c02430.

(22) Zuo, T.; Walther, F.; Teo, J. H.; Rueß, R.; Wang, Y.; Rohnke, M.; Schröder, D.; Nazar, L. F.; Janek, J. Impact of the Chlorination of Lithium Argyrodites on the Electrolyte/Cathode Interface in Solid-State Batteries. *Angew. Chem. Int. Ed.* **2023**, *62* (7), e202213228. https://doi.org/10.1002/anie.202213228.

(23) Temprano, I.; Carrasco, J.; Bugnet, M.; Lucas, I. T.; Zhou, J.; Weatherup, R. S.; O'Keefe, C. A.; Ruff, Z.; Xu, J.; Folastre, N.; Wang, J.; Gajan, A.; Demortière, A. Advanced Methods for Characterizing Battery Interfaces: Towards a Comprehensive Understanding of Interfacial

Evolution in Modern Batteries. *Energy Storage Mater.* **2024**, *73*, 103794. https://doi.org/10.1016/j.ensm.2024.103794.

(24) Kim, J.; Lee, D.; Nam, C.; Chung, J.; Koo, B.; Kim, N.; Lim, J. Energy Material Analysis via In-Situ/Operando Scanning Transmission X-Ray Microscopy: A Review. *J. Electron Spectrosc. Relat. Phenom.* **2023**, *266*, 147337. https://doi.org/10.1016/j.elspec.2023.147337.

(25) Lim, J.; Li, Y.; Alsem, D. H.; So, H.; Lee, S. C.; Bai, P.; Cogswell, D. A.; Liu, X.; Jin, N.; Yu, Y.; Salmon, N. J.; Shapiro, D. A.; Bazant, M. Z.; Tyliszczak, T.; Chueh, W. C. Origin and Hysteresis of Lithium Compositional Spatiodynamics within Battery Primary Particles. *Science* **2016**, *353* (6299), 566–571. https://doi.org/10.1126/science.aaf4914.

(26) Sun, T.; Sun, G.; Yu, F.; Mao, Y.; Tai, R.; Zhang, X.; Shao, G.; Wang, Z.; Wang, J.; Zhou, J. Soft X-ray Ptychography Chemical Imaging of Degradation in a Composite Surface-Reconstructed Li-Rich Cathode. *ACS Nano* **2021**, *15* (1), 1475–1485. https://doi.org/10.1021/acsnano.0c08891.

(27) Sun, G.; Wang, H.; Lee, C.; Zhu, Q.; Gao, L.; Hsieh, S.; Shao, Y.; Ishii, H.; Zhou, J.; Wang, J.; Wang, Z. Visualization of Thermal-Induced Degradation Pathways of High-Ni Cathode: A Comparative Study in Solid Chloride and Liquid Electrolytes. *Adv. Mater.* **2025**, e10392. https://doi.org/10.1002/adma.202510392.

(28) Yan, S.; Abouali, S.; Yim, C.-H.; Zhou, J.; Wang, J.; Baranova, E. A.; Weck, A.; Thangadurai, V.; Merati, A.; Abu-Lebdeh, Y. Revealing the Role of Liquid Electrolytes in Cycling of Garnet-Based Solid-State Lithium-Metal Batteries. *J. Phys. Chem. C* **2022**, *126* (33), 14027–14035. https://doi.org/10.1021/acs.jpcc.2c02074.

(29) Yan, S.; Yim, C.-H.; Zhou, J.; Wang, J.; Abouali, S.; Baranova, E. A.; Weck, A.; Thangadurai, V.; Merati, A.; Abu-Lebdeh, Y. Elucidating the Origins of Rapid Capacity Fade in Hybrid Garnet-Based Solid-State Lithium Metal Batteries. *J. Phys. Chem. C* **2023**, *127* (51), 24641–24650. https://doi.org/10.1021/acs.jpcc.3c05419.

(30) Lou, S.; Liu, Q.; Zhang, F.; Liu, Q.; Yu, Z.; Mu, T.; Zhao, Y.; Borovilas, J.; Chen, Y.; Ge, M.; Xiao, X.; Lee, W.-K.; Yin, G.; Yang, Y.; Sun, X.; Wang, J. Insights into Interfacial Effect and Local Lithium-Ion Transport in Polycrystalline Cathodes of Solid-State Batteries. *Nat. Commun.* **2020**, *11* (1), 5700. https://doi.org/10.1038/s41467-020-19528-9.

(31) Alt, C. D.; Müller, N. U. C. B.; Riegger, L. M.; Aktekin, B.; Minnmann, P.; Peppler, K.; Janek, J. Quantifying Multiphase SEI Growth in Sulfide Solid Electrolytes. *Joule* **2024**, *8* (10), 2755–2776. https://doi.org/10.1016/j.joule.2024.07.006.

(32) Zuo, T.-T.; Rueß, R.; Pan, R.; Walther, F.; Rohnke, M.; Hori, S.; Kanno, R.; Schröder, D.; Janek, J. A Mechanistic Investigation of the $Li_{10}GeP_2S_{12}|LiNi_{1-x-y}Co_xMn_yO_2$ Interface Stability in All-Solid-State Lithium Batteries. *Nat. Commun.* **2021**, *12* (1), 6669. https://doi.org/10.1038/s41467-021-26895-4.

(33) Achkar, A. J.; Regier, T. Z.; Wadati, H.; Kim, Y.-J.; Zhang, H.; Hawthorn, D. G. Bulk Sensitive X-Ray Absorption Spectroscopy Free of Self-Absorption Effects. *Phys. Rev. B* **2011**, *83* (8), 081106. https://doi.org/10.1103/physrevb.83.081106.

(34) Banerjee, A.; Tang, H.; Wang, X.; Cheng, J.-H.; Nguyen, H.; Zhang, M.; Tan, D. H. S.; Wynn, T. A.; Wu, E. A.; Doux, J.-M.; Wu, T.; Ma, L.; Sterbinsky, G. E.; D'Souza, M. S.; Ong, S. P.; Meng, Y. S. Revealing Nanoscale Solid–Solid Interfacial Phenomena for Long-Life and High-

Energy All-Solid-State Batteries. *ACS Appl. Mater. Interfaces* **2019**, *11* (46), 43138–43145. https://doi.org/10.1021/acsami.9b13955.

(35) Ramesh, N.; Banerjee, H.; Swallow, J. E. N.; Björklund, E.; Dean, A.; Didwal, P.; Fraser, M.; Phelan, C. M. E.; An, L.; Singh, J.; Lewis, J.; Song, W.; House, R. A.; Morris, A. J.; Weatherup, R. S.; Nicholls, R. J. Atomistic Interpretation of the Oxygen K-Edge X-Ray Absorption Spectra of Layered Li-Ion Battery Cathode Materials. *Chem. Mater.* **2024**, *36* (22), 11051–11064. https://doi.org/10.1021/acs.chemmater.4c01870.

(36) Tian, C.; Nordlund, D.; Xin, H. L.; Xu, Y.; Liu, Y.; Sokaras, D.; Lin, F.; Doeff, M. M. Depth-Dependent Redox Behavior of $LiNi_{0.6}Mn_{0.2}Co_{0.2}O_2$. *J. Electrochem. Soc.* **2018**, *165* (3), A696–A704. https://doi.org/10.1149/2.1021803jes.

(37) Fleet, M. E. XANES Spectroscopy of Sulfur in Earth Materials. *Can. Miner.* **2005**, *43* (6), 1811–1838. https://doi.org/10.2113/gscanmin.43.6.1811.

(38) Gilbert, B.; Perfetti, L.; Fauchoux, O.; Redondo, J.; Baudat, P.-A.; Andres, R.; Neumann, M.; Steen, S.; Gabel, D.; Mercanti, D.; Ciotti, M. T.; Perfetti, P.; Margaritondo, G.; Stasio, G. D. Spectromicroscopy of Boron in Human Glioblastomas Following Administration of $Na_2B_{12}H_{11}SH$. *Phys. Rev. E* **2000**, *62* (1), 1110–1118. https://doi.org/10.1103/physreve.62.1110.

(39) Komatsu, H.; Banerjee, S.; Chandrappa, M. L. H.; Qi, J.; Radhakrishnan, B.; Kuwata, S.; Sakamoto, K.; Ong, S. P. Interfacial Stability of Layered $LiNi_xMn_yCo_{1-x-y}O_2$ Cathodes with Sulfide Solid Electrolytes in All-Solid-State Rechargeable Lithium-Ion Batteries from First-Principles Calculations. *J. Phys. Chem. C* **2022**, *126* (41), 17482–17489. https://doi.org/10.1021/acs.jpcc.2c05336.

(40) Farzanian, S.; Mercado, J. V.; Shozib, I.; Sivadas, N.; Lacivita, V.; Wang, Y.; Tu, Q. H. Mechanical Investigations of Composite Cathode Degradation in All-Solid-State Batteries. *ACS Appl. Energy Mater.* **2023**, *6* (18), 9615–9623. https://doi.org/10.1021/acsaem.3c01681.

(41) Jung, R.; Metzger, M.; Maglia, F.; Stinner, C.; Gasteiger, H. A. Oxygen Release and Its Effect on the Cycling Stability of $LiNi_xMn_yCo_zO_2$ (NMC) Cathode Materials for Li-Ion Batteries. *J. Electrochem. Soc.* **2017**, *164* (7), A1361–A1377. https://doi.org/10.1149/2.0021707jes.

(42) Hitchcock, A. P. Analysis of X-Ray Images and Spectra (aXis2000): A Toolkit for the Analysis of X-Ray Spectromicroscopy Data. *J. Electron Spectrosc. Relat. Phenom.* **2023**, *266*, 147360. https://doi.org/10.1016/j.elspec.2023.147360.

(43) Ravel, B.; Newville, M. ATHENA, ARTEMIS, HEPHAESTUS: Data Analysis for X-Ray Absorption Spectroscopy Using IFEFFIT. *J. Synchrotron Radiat.* **2005**, *12* (4), 537–541. https://doi.org/10.1107/s0909049505012719.

TOC GRAPHICS

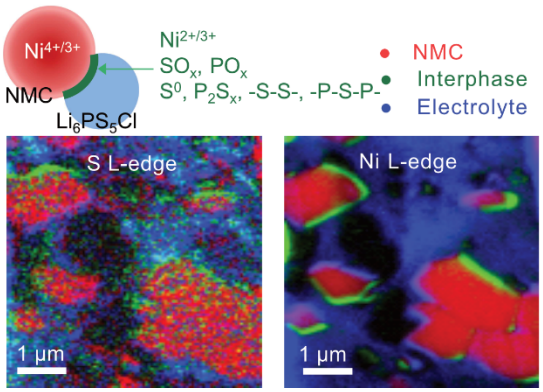

This work directly visualizes interfacial degradation in NMC-argyrodite composite cathodes using STXM chemical mapping. Higher voltage cycling drives Ni reduction and sulfide oxidation at the NMC interface, forming S^0 and SO_x^{2-} species, while the bulk electrolyte remains stable. The resulting interphase growth increases impedance and accelerates capacity fade.